

*The impact of two coupled cirrus
microphysics-radiation parameterizations
on the temperature and specific humidity
biases in the tropical tropopause layer in a
climate model*

Article

Accepted Version

Baran, A. J., Hill, P. ORCID: <https://orcid.org/0000-0002-9745-2120>, Walters, D., Hardiman, S. C., Furtado, K., Field, P. R. and Manners, J. (2016) The impact of two coupled cirrus microphysics-radiation parameterizations on the temperature and specific humidity biases in the tropical tropopause layer in a climate model. *Journal of Climate*, 29 (14). pp. 5299-5316. ISSN 1520-0442 doi: 10.1175/JCLI-D-15-0821.1 Available at <https://centaur.reading.ac.uk/65666/>

It is advisable to refer to the publisher's version if you intend to cite from the work. See [Guidance on citing](#).

Published version at: <http://dx.doi.org/10.1175/JCLI-D-15-0821.1>

To link to this article DOI: <http://dx.doi.org/10.1175/JCLI-D-15-0821.1>

Publisher: American Meteorological Society

including copyright law. Copyright and IPR is retained by the creators or other copyright holders. Terms and conditions for use of this material are defined in the [End User Agreement](#).

www.reading.ac.uk/centaur

CentAUR

Central Archive at the University of Reading

Reading's research outputs online



AMERICAN METEOROLOGICAL SOCIETY

Journal of Climate

EARLY ONLINE RELEASE

This is a preliminary PDF of the author-produced manuscript that has been peer-reviewed and accepted for publication. Since it is being posted so soon after acceptance, it has not yet been copyedited, formatted, or processed by AMS Publications. This preliminary version of the manuscript may be downloaded, distributed, and cited, but please be aware that there will be visual differences and possibly some content differences between this version and the final published version.

The DOI for this manuscript is doi: 10.1175/JCLI-D-15-0821.1

The final published version of this manuscript will replace the preliminary version at the above DOI once it is available.

If you would like to cite this EOR in a separate work, please use the following full citation:

Baran, A., P. Hill, D. Walters, S. Hardiman, K. Furtado, P. Field, and J. Manners, 2016: The Impact of Two Coupled Cirrus Microphysics-Radiation Parameterizations on the Temperature and Specific Humidity Biases in the Tropical Tropopause Layer in a Climate Model. *J. Climate*. doi:10.1175/JCLI-D-15-0821.1, in press.



**The Impact of Two Coupled Cirrus Microphysics-Radiation Parameterizations on
the Temperature and Specific Humidity Biases in the Tropical Tropopause Layer in
a Climate Model**

Anthony J. Baran

Met Office, Exeter, Devon, U. K.

Peter Hill

Dept of Meteorology, University of Reading, Reading, U. K.

David Walters

Met Office, Exeter, Devon, U. K.

Steven C. Hardiman

Met office, Exeter, Devon, U. K.

Kalli Furtado

Met Office, Exeter, Devon, U. K.

Paul R. Field

Met Office, Exeter, Devon, U. K.

The University of Leeds, Leeds, U. K.

James Manners

Met Office, Exeter, Devon, U. K.

7th April 2016

Revised for the Journal of Climate

Corresponding author address: Dr Anthony J. Baran, Met Office, Cordouan 2, FitzRoy
Road, Exeter, Devon EX1 3PB, UK.

E-mail: anthony.baran@metoffice.gov.uk

ABSTRACT

The impact of two different coupled cirrus microphysics-radiation parameterizations on the zonally averaged temperature and humidity biases in the tropical tropopause layer (TTL) of a Met Office climate model configuration is assessed. One parameterization is based on a linear coupling between a model prognostic variable, the ice mass mixing ratio, q_i , and the integral optical properties. The second is based on the integral optical properties being parameterized as functions of q_i and temperature, T_c , where the mass coefficients (i.e. scattering and extinction) are parameterized as nonlinear functions of the ratio between q_i and T_c . The cirrus microphysics parameterization is based on a moment estimation parameterization of the particle size distribution (PSD), which relates the mass moment (i.e. second moment if mass is proportional to size raised to the power of 2) of the PSD to all other PSD moments through the magnitude of the second moment and T_c . This same microphysics PSD parameterization is applied to calculate the integral optical properties used in both radiation parameterizations and, thus, ensures PSD and mass consistency between the cirrus microphysics and radiation schemes.

In this paper, the temperature-non-dependent and temperature-dependent parameterizations are shown to increase and decrease the zonally averaged temperature biases in the TTL by about 1 K, respectively. The temperature-dependent radiation parameterization is further demonstrated to have a positive impact on the specific humidity biases in the TTL, as well as decreasing the shortwave and longwave biases in the cloudy radiative effect. The temperature-dependent radiation parameterization is shown to be more consistent with TTL and global radiation observations.

1. Introduction

It is well known that cirrus makes an important contribution to the radiative balance of the tropical tropopause layer (TTL) through its temperature, spatial distributions, opacity, and composition. Moreover, it influences the water vapor concentration in the stratosphere (Heymsfield 1986; Sassen et al. 1989; McFarquhar et al. 2000; Corti et al. 2006; Wang and Dessler 2006; Stubenrauch et al. 2007; Jensen et al. 2008; Mace et al. 2009; Yang et al. 2010; Schwartz and Mace 2010; Taylor et al. 2011; Zhou et al. 2014; Hong and Liu 2015; Hardiman et al. 2015, and references therein).

Typical TTL cirrus will efficiently trap outgoing longwave radiation from the surface and atmosphere, generally leading to a warming of the surface, and absorb incoming shortwave radiation at near-infrared wavelengths, generally leading to a local heating of the upper troposphere (Liou 1986; Liou 2005; Edwards et al. 2007; Baran 2009; Taylor et al. 2011; Baran 2012; Yi et al. 2013; Zhou et al. 2014; Hong and Liu 2015; Yang et al., 2015; Hardiman et al. 2015). The balance between cirrus warming or cooling the upper troposphere depends on its visible optical depth, as shown by Hong and Liu (2015), who demonstrated that cirrus with visible optical depths less than unity leads to a net heating of the upper troposphere, whilst optically thicker cirrus results in a net cooling of the upper troposphere. Moreover, subvisual cirrus occurs in the TTL, as found by Lawson et al. (2008), and Lee et al. (2009) showed that these clouds may exert a net radiative effect on the order of about 1.1 Wm^{-2} .

In general, the role of cirrus in either heating or cooling the TTL depends not only

on the visible optical depth but also on the microphysics and the scattering and absorption properties of atmospheric ice (Baran et al. 2014a; Yang et al. 2015, and references therein). There have been aircraft campaigns which have examined the ice microphysics composition of the TTL. In the study by Heymsfield (1986), the common occurrence of trigonal particles was reported but more recent studies by Lawson et al. (2008) have found few occurrences of trigonal ice particles. In the study by McFarquhar et al. (2000), they found habit mixtures comprising 50% of hexagonal columns and trigonal ice crystals in the subvisual TTL cirrus they studied. Meanwhile, Lawson et al. (2008) found the occurrence of quasi-spherical ice particles to be the most common particle type for all crystal sizes. However, it is uncertain as to whether these particles are actually quasi-spherical due to the limiting resolving power of the microphysics instrumentation used at the time; therefore, the appearance of quasi-sphericity could be due to diffractive and optical effects, as noted by Cotton et al. (2010) and references therein. On the other hand, these particles could be quasi-spherical, but instruments are required that can adequately resolve these ice crystals of an uncertain shape, such as the small ice detector described in Ulanowski et al. (2006). For crystal sizes greater than 65 μm , Lawson et al. (2008) found habit mixtures comprising mostly hexagonal plates and irregular ice crystals. In the study by Jensen et al. (2008) they noted the occurrence of hexagonal plate aspect ratios of 6:1 of nearly 100 μm in size near the TTL, which were reported to be unassociated with deep tropical convection. The more recent Airborne Tropical Tropopause Experiment (ATTREX) reported by Jensen et al. (2015) found bullet rosettes to be commonly occurring with little evidence of aggregated ice crystals in the cirrus cases

1 they sampled. The two particle size distributions shown in Jensen et al. (2015) extend
2 to maximum dimensions of about 50 μm and almost 200 μm , at temperatures of <
3 195 K and between about 195 and less than 210 K, respectively. Meanwhile, Lawson
4 et al. (2008) report particle distributions extending to 165 μm in the subvisual TTL
5 cirrus they sampled, which contrasts with the study of McFarquhar et al. (2000), who
6 found that particle maximum dimensions did not extend to beyond 50 μm .

7 Determining the habit mixtures and particle distributions in TTL cirrus is important,
8 as the choice of assumed particle distributions in climate models will influence their
9 predicted radiative effect of cirrus. For instance, in the study of Mitchell et al. (2008)
10 they show that by assuming two different parameterizations of the small ice mode,
11 the shortwave radiative effect differences in the annual zonally averaged fluxes at
12 top-of-atmosphere in the tropics can be up to about -25 Wm^{-2} . They also show that
13 the longwave differences in the tropics can be up to 20 Wm^{-2} . Clearly, from the
14 studies cited above, there is uncertainty as to the most general ice microphysics
15 composition in the TTL to assume in models, in turn, this will affect climate model
16 simulations of the TTL, as differing climate models assume dissimilar microphysics
17 properties, which may lead to an excess in TTL warming or cooling (Hardiman et al.
18 2015). Further campaigns in the TTL are necessary if such uncertainties reported by
19 Hardiman et al. (2015) are to be reduced in climate models. However, recent TTL
20 process studies by Hardiman et al. (2015) have shown that physically improved
21 climate model parameterizations do not necessarily improve simulations of the TTL.
22 For example, recent parameterizations of cirrus microphysics and bulk optical
23 properties by Furtado et al. (2015) and Baran et al. (2014a), respectively, were shown

1 to increase the temperature and specific humidity biases in the TTL in recent global
2 configurations of the Met Office Unified Model (MetUM). In this paper, the physical
3 reasons are explored as to why the Baran et al. (2014b) parameterizations, hereinafter
4 referred to as B014b, increased the TTL temperature bias in the climate model. This
5 paper also presents a new bulk optical property parameterization of cirrus that is
6 demonstrated to provide a more accurate simulation of the TTL in the MetUM as well
7 as an improved representation of MetUM simulations of the cloudy shortwave and
8 longwave radiative effects. The paper is organised as follows: Section 2 describes the
9 bulk optical property parameterization and its accuracy, and includes comparisons
10 between the new and the B014b parameterizations. Section 3 briefly describes a
11 baseline MetUM configuration and compares the impact of the new and B014b
12 parameterizations on this configuration against both observations and analyses.
13 Section 4 discusses the results.

14 **2. The parameterization**

15 The parameterization presented in this paper is based on the ensemble model of cirrus
16 ice crystals fully described in Baran and Labonnote (2007), whereby the bulk optical
17 properties are derived by averaging habit-dependent, single-scattering properties over an
18 assumed PSD; a figure of the model is shown in Fig. 2 in B014b. A brief description of
19 the model is given here. The ensemble model consists of six shapes, and these are a
20 hexagonal ice column of an assumed aspect ratio (AR) of unity, the six-branched bullet
21 rosette, and then hexagonal monomers are randomly attached to build four ice aggregate
22 models, which consist of three-, five-, eight- and, finally, ten-branched hexagonal ice
23 aggregates. The latter aggregate models can cover the largest ice crystal sizes found in the

1 PSD, whilst the former members can populate the smaller end of the ice crystal PSD.
2 Alternatively, weights can be assigned to each member of the ensemble model at each
3 PSD bin size to compute the bulk optical properties. Here, use is also made of the same
4 bulk ice optical property database that was used to develop the B014b parameterization.
5 The database is composed of the following bulk optical properties: the extinction and
6 scattering coefficients, the single-scattering albedo, ω_0 , and the asymmetry parameter, g .
7 These bulk optical properties are defined by Eqs. (1–3) in B014b, and the same
8 definitions are used in this paper. A full description of that database can be found in
9 B014b and in Baran et al. (2014a), hereinafter referred to as B014a. However, brief
10 descriptions of the bulk optical property database and its experimental validation are
11 given here. The database described in B014a consists of 20662 values of ice water
12 content (IWC) and T_c , which were compiled from a number of cirrus field campaigns
13 described in Baran et al. (2011a), and these in-situ campaigns were predominantly
14 located between northern Europe and the tropics. However, most of the in-situ IWC
15 values that were compiled by Baran et al. (2011a) were not obtained at temperatures
16 colder than -60°C . Due to this lack of in-situ ice microphysics measurements down to
17 temperatures as low as -80°C , in B014a, IWC values were randomly selected from
18 temperatures warmer than -60°C and placed at temperatures between -60 and -80°C . In
19 this way, the IWC and T_c space was built up to 20662 values, which ranged between
20 about 3.0×10^{-3} and about $10^{-9} \text{ kg m}^{-3}$, and between about -80 and 0°C , respectively. This
21 range in IWC and T_c is sufficient to cover the range in IWC and T_c values that are likely
22 to be predicted in the MetUM.

23 In B014a and B014b, the IWC and T_c values were related to the PSD through a

1 moment estimation parameterization of the PSD due to Field et al. (2007), and this
2 parameterization is further described below. The IWC– T_c generated PSDs were
3 previously applied to the ensemble model single-scattering properties described in B014a
4 to obtain the cirrus bulk optical properties used in B014b at 145 wavelengths between
5 0.20 and 120 μm . The same bulk ice optical properties utilized in B014b are used in this
6 paper.

7 The coupled IWC– T_c bulk ice optical properties used in this paper have been validated
8 using a variety of aircraft and space-based solar and infrared radiometric measurements.
9 For instance, in B014a the ensemble model bulk ice optical properties were applied to a
10 fast radiative transfer model to simulate very high-resolution solar (between about 3.4
11 and 4.1 μm) and infrared (between about 8.0 and 12.0 μm) aircraft-based brightness
12 temperature measurements obtained from directly above midlatitude cirrus of visible
13 optical depth varying between about 0.03 and 0.06. It is shown in the paper that the solar
14 and infrared brightness temperature measurements were mostly simulated to within ± 2
15 and ± 1 K, respectively. Note also that the lower visible optical depth of 0.03 is generally
16 taken as the upper limit for “subvisual” cirrus, as defined by Sassen and Cho (1992).
17 Moreover, B014a also showed that the same ensemble microphysical model could
18 forward model deep frontal cirrus effective radar reflectivity at 35 GHz and microwave
19 brightness temperatures at 190 GHz to generally within ± 2 dBZ_e and ± 2 K, respectively.
20 Thus, B014a showed that in the case of the solar and infrared measurements, the same
21 microphysical model can be consistently applied across the spectrum using a full set of
22 optical properties (i.e. the scattering phase function and integral optical properties) to
23 simulate those observations. Meanwhile, Sourdeval et al. (2015) demonstrated that the

1 same ensemble model bulk ice optical properties used in B014a could also replicate
2 Cloud-Aerosol Lidar with Orthogonal Polarization (CALIOP) and in-situ polar
3 nephelometer measurements of the volume extinction coefficient of midlatitude cirrus to
4 generally within the standard deviation of both CALIOP and polar nephelometer
5 measurements. The in-situ and CALIOP volume extinction coefficients varied between
6 less than about 0.2 and 1.4 km⁻¹, at the wavelengths of 0.532 and 0.80 μm, respectively.
7 The ensemble model's predicted bulk optical properties have also been globally validated
8 by Vidot et al. (2015) and Letu et al. (2015).

9 In Vidot et al. (2015) it is shown that an equivalent weighting of 0.30, 0.30, 0.10, 0.20,
10 and 0.10 applied to each of the ensemble habit extinction and scattering coefficients at
11 each bin size of the Field et al. (2007) PSD parameterization best simulated cirrus
12 infrared brightness temperature measurements from the Imaging Infrared Radiometer
13 (IIR) instrument at wavelengths of 8.65, 10.60 and 12.05 μm. The combined mean
14 brightness temperature bias using the weighted model optical properties was found to be
15 only 0.43 K with a standard deviation of 6.85 K for visible optical depths between 0.03
16 and 4.0. The IIR brightness temperature simulations were based on more than 26000
17 profiles of IWC from the 2C-ICE and DARDAR products (Deng et al. 2010; Delanöe and
18 Hogan 2010). The IWC product profiles and atmospheric profiles (the latter profiles came
19 from the European Centre for Medium Range Weather Forecasts and were colocated with
20 CALIOP) were located between the latitudes of about ±60° and at altitudes between about
21 440 and 50 hPa, thus covering the region of the TTL, and most of the profiles were
22 located in the tropics. Meanwhile, Letu et al. (2015) used global observations from the
23 Polarization and Directionality of the Earth's Reflectances-3 (POLDER-3) measurements

on board the Polarization and Anisotropy of Reflectances for Atmospheric Sciences coupled with Observations from a Lidar (PARASOL) to show that the ensemble model's predicted ice cloud solar optical depths at a wavelength of $0.865\ \mu\text{m}$ best minimized differences between observations, with all ice crystal models considered. The POLDER-3 analysis of Letu et al. (2015) is based on 589246 pixels, with each pixel size being approximately $6\ \text{km} \times 6\ \text{km}$. In most pixels the scattering angle range covered is between 60° and 160° , and in some pixels the scattering angle range covered is between 160° and 180° . The pixels were located between the latitudes of about $\pm 90^\circ$, but the vast majority of pixels were located at latitudes between about $\pm 60^\circ$. The data covers the period between the 20th to 22nd of March, June, September and December 2008. Therefore, all meteorological seasons are covered in the time period studied by Letu et al. (2015), and the study is, thus far, the most comprehensive and consistent analysis of POLDER-3 global data. Given the preceding evidence, the ensemble model bulk ice optical properties have been sufficiently validated globally to apply to a parameterization of cirrus optical properties in a climate model. Such validation exercises described above are necessary to carry out to show that the full set of optical properties are consistent with measurements from across the spectrum in order to provide confidence in their applicability to climate models. As a further example of this validation approach, see for example, the paper by Holz et al. (2015).

The PSDs applied to the ensemble model single-scattering properties in the preceding literature assumed the Field et al. (2007) moment estimation parameterization of the PSD, hereinafter referred to as F07. A full derivation of the PSD parameterization is given in F07, but a brief description is given here. The Field

1 et al. (2007) parameterization is based on 10000 in-situ measurements of the PSD and
 2 IWC, which were measured between the temperatures of 0°C and -60°C during a
 3 number of cirrus field campaigns located in the midlatitudes and tropics. The
 4 parameterization is based on the moments of the PSD, given by the integral product
 5 of D^n and $f(D)$, where D is the maximum dimension of the ice crystal and $f(D)$ is the
 6 PSD, which gives the particle number concentration at each D , and $n \geq 0$. Therefore,
 7 the zeroth moment (i.e. $n=0$) is the total number concentration of particles per unit
 8 volume of cloudy air. The PSD parameterization is related to the total IWC through
 9 some assumed relationship between mass and D , where in the case of aggregating ice
 10 crystals the mass of ice $\propto D^2$ (Westbrook et al. 2004; Cotton et al. 2013, and
 11 references therein). The other moments of the PSD are related to the 2nd moment (M_2)
 12 through a relationship of the form $M_n = \sigma_n M_2^{\beta_n}$, where σ_n and β_n are functions of T_c .
 13 Therefore, given all M_n , the full PSD can be estimated from the IWC and T_c values
 14 via an assumed mass–dimensional relationship. It should be noted here that to reduce
 15 the impact of ice crystal shattering on the PSD parameterization, the in-situ PSDs in
 16 F07 were filtered by using the measured inter-arrival times of the ice crystals as
 17 described in F07 and in Field et al. (2006), and ice crystals with $D < 100 \mu\text{m}$ were
 18 ignored. However, the PSD parameterization does not ignore the shape of the ice
 19 crystal PSD at $D < 100 \mu\text{m}$, but instead assumes an exponential PSD (Field and
 20 Heymsfield 2003) that is added to a modified gamma distribution at an ice crystal size
 21 of about $100 \mu\text{m}$. The degree to which in-situ PSDs are skewed due to ice crystal
 22 shattering has more recently been studied by Korolev et al. (2013). In that paper, they
 23 found that if filtering alone is applied without any modifications to the in-situ

1 microphysics probes on board aircraft, such as the use of anti-shatter tips, the PSD
2 becomes significantly skewed from the best measured PSD at $D \leq 200\text{--}175\text{ }\mu\text{m}$,
3 where the best measured PSDs were determined using both anti-shatter tips and
4 filtering. Korolev et al. (2013) state that the precise ice crystal size at which
5 significant divergence from the best-estimated PSD occurs cannot as yet be
6 determined due to insufficient statistical sampling of ice clouds. In other words, there
7 are too few cirrus field campaigns on which to base firm conclusions. Therefore, it is
8 currently unknown as to the degree to which the F07 parameterization has been
9 affected by the shattering of ice. However, this parameterization is more
10 representative of cirrus PSDs than the Houze et al. (1979) PSD parameterization,
11 which is the current assumption in the MetUM operational model. The Houze et al.
12 (1979) parameterization is based on 37 in-situ PSDs, 90% of which were measured at
13 temperatures warmer than -30°C . Currently, within the operational MetUM, the
14 Houze et al. (1979) estimated PSD is kept constant at temperatures colder than -35°C .
15 This assumption means that at much colder temperatures, such as those that occur
16 within the TTL region, there will be orders of magnitude more frequently occurring
17 large ice crystals than there should be. This has clear implications for the assumed fall
18 speed of ice crystals within the MetUM model, which must be artificially increased to
19 several ms^{-1} to accommodate space-based radiometric shortwave and outgoing
20 longwave measurements of flux at top-of-atmosphere (TOA).

21 The F07 parameterization has been experimentally validated by Baran et al.
22 (2011b) and Furtado et al. (2015). In Baran et al. (2011b) the moment estimated PSD
23 was found to fit well to several cases of averaged in-situ measured tropical PSDs. For

1 several cases of midlatitude cirrus Furtado et al. (2015) compared the F07 moments to
 2 in-situ measured moments, whilst ignoring particles less than 100 μm in size, due to
 3 the current uncertainties in measuring the size of small ice at $D < 100 \mu\text{m}$, and found
 4 good correlations between the parameterization and measurements for all cases
 5 considered. However, poor correlations emerged in that study when the moments
 6 predicted by the Houze et al. (1979) parameterization were compared against the in-
 7 situ derived moments. The study of Furtado et al. (2015) emphasizes that the F07
 8 parameterization is a better representation of the ice PSD to apply to climate models
 9 in general than the Houze et al. (1979) parameterization. This last statement is
 10 especially true in the TTL, given the above description of the Houze et al. (1979)
 11 parameterization.

12 Given that the F07 PSDs are related to a model prognostic variable (i.e. the mass
 13 carrying moment M_2) and this varies as a function of T_c , given that the ensemble model
 14 single-scattering properties have been integrated over these PSDs, the bulk ice optical
 15 properties can also be directly related to the climate model prognostic variable IWC (i.e.
 16 $m(D)=\text{constant} \times D^2$, where m is the mass in units of kg) and T_c or just IWC (as is the
 17 case in B014b). The behavior of the 20662 bulk ice optical properties, ω_0 and g , in M_2 – T_c
 18 space, is shown in Figs. 1a and 1b, respectively, at a wavelength of 1.575 μm . This
 19 wavelength is chosen as an example to show the variation of the bulk ice optical
 20 properties in the full space used for the later parameterizations. In Fig. 1a, it is shown that
 21 ω_0 varies between the values of 0.7 and 1.0, at the coldest temperature values, down to
 22 about -80°C and $M_2 \sim 10^{-5} \text{ m}^{-1}$, and ω_0 is near unity. At these values of M_2 and T_c , the PSD
 23 is very narrow and will be largely composed of small ice crystals with much fewer

occurring large ice crystals; therefore at this wavelength the smaller ice crystals will
 efficiently scatter incident radiation. At much larger values of M_2 and at much warmer
 temperatures, at 0.01 m^{-1} and -15°C , respectively, the value of ω_0 decreases to a value of
 about 0.8. At such M_2 and T_c values, the PSD becomes much broader than previously,
 with much more frequently occurring large ice crystals, which at this wavelength will
 absorb incident radiation, thereby decreasing ω_0 . The converse behavior is shown, at the
 same values of M_2 and T_c , for g in Fig. 1b, where g has the corresponding values of about
 0.78 and 0.88. The reasons for these values are the same as those given for the behavior
 of ω_0 . Figures 1a–1b show that the spatial distribution of ω_0 and g is physically to
 expectation and would be a similar distribution if the optical properties were plotted as a
 function of some characteristic size. Here, we demonstrate this using the characteristic
 size usually assumed in radiation schemes in climate models, which is the mean effective
 dimension, D_{eff} , defined after Foot (1988) as:

$$D_{\text{eff}} = \frac{\text{mass}_t}{\rho A_t} \quad (1)$$

where in Eq. (1) mass_t and A_t are the total mass and orientation-averaged projected area
 of the PSD, respectively, and ρ is the density of solid ice. Here, we assume that $\rho=1000$
 kg m^{-3} to keep units in Eq. (1) consistent, hence the units of mass_t and A_t being in SI.
 Firstly, we show that the moment M_2 can easily be related to D_{eff} , as shown in Fig. 2,
 where in Fig. 2, as an example, we assume that the mass_t and A_t are computed from the
 first member of the ensemble model, which is the hexagonal ice column of $\text{AR}=1.0$. As
 can be seen from Fig. 2, the 2nd moment or, equivalently, IWC (by assuming some mass–
 D relationship) could easily be related to D_{eff} as a function of T_c or just by relating IWC

directly to D_{eff} by using some fitting procedure. Indeed, this latter approach was used by
 McFarquhar et al. (2003), who parameterized IWC explicitly as a function of an effective
 radius (D_{eff} can be related to the effective radius, r_{eff} , by $r_{\text{eff}} = (3/4) \times D_{\text{eff}}$). Therefore, the
 bulk ice optical properties can also be easily parameterized as a function of M_2 or IWC
 and T_c , as is done in B014b (i.e. IWC alone) and in this paper (i.e. IWC and T_c). We
 note that, for aggregating ice crystals both mass and diameter are proportional to D^2 , so
 D_{eff} becomes independent of IWC. A further characteristic size could also be defined,
 such as the ratio between the 3rd and 2nd moments of the PSD. If the 2nd moment is the
 mass carrying moment M_2 , this characteristic size is the mean mass-weighted size, D_{mmw} .
 The relationship between D_{eff} and D_{mmw} is characterized by Figs. 3a–3b, respectively,
 which show the variation of ω_0 at a wavelength of 1.575 μm as a function of the
 characteristic sizes and T_c for all 20662 F07 PSDs. In the case of D_{eff} , in the figures, the
 same definitions are used as above. The figure shows that D_{eff} is simply some multiple of
 D_{mmw} and the spatial distribution of ω_0 in the spaces of characteristic size— T_c is exactly
 the same. Furthermore, the distribution of ω_0 shown in Figs. 3a–3b is relatable to Fig.
 1a. That is, at the same T_c values of -80°C and -15°C , small and large characteristic
 sizes can be chosen to give the same values of ω_0 for the same values of M_2 assumed
 above. The above figures illustrate that there is a choice to be made as to how the bulk
 ice optical properties are parameterized in climate models.

As is done in B014b and in this paper, we avoid relating the bulk ice optical
 properties to D_{eff} as is traditionally done. Instead, our choice is to relate the optical
 properties directly to climate model prognostic variables such as M_2 /IWC. This is because
 in climate models, D_{eff} is generally diagnosed in the radiation scheme and the D_{eff} in the

1 radiation scheme is different from the D_{eff} in the cloud physics scheme of a climate model
2 because different PSDs are usually assumed. In the approach adopted by B014b and in
3 this paper, we ensure that the PSDs generated through the F07 parameterization in the
4 cloud physics scheme in the climate model are the *same* as those used in the radiation
5 scheme, thus providing internal physical consistency within the climate model. In the
6 traditional approach, this physical internal consistency is generally currently lost. Internal
7 physical consistency could be satisfied using the traditional approach if D_{eff} were
8 determined from the PSDs within the cloud physics scheme of the climate model and
9 these values passed to the radiation scheme. In this way, the effective size then becomes
10 consistent between the two schemes. However, this recovery of physical consistency
11 requires an extra step within the climate model. Here, we prefer to avoid such an
12 unnecessary step. It should also be noted that from Eq. (1), the integral over the mass
13 requires some mass–D relationship to be applied. However, this mass–D relationship will
14 obviously change depending on the choice of habit models; as a consequence, this has the
15 potential to change the spatial distribution of ω_0 shown in Fig. 3a. However, in the
16 approach adopted here, the mass of ice predicted by the climate model cannot change
17 and, thus, will always be the same mass of ice between the cloud physics and radiation
18 schemes.

19 In this paper, to generate the PSDs, the F07 moments are generated while assuming
20 the recommended Furtado et al. (2015) mass–dimensional pre-factor and exponent values
21 of 0.0257 and 2.0, respectively, which were derived by Cotton et al. (2013), and by using
22 the 20662 IWC estimates and in-cloud temperature measurements compiled by B014a.
23 Note that this mass–dimensional relationship is the same as that assumed by Hardiman et

al. (2015), and was used by Vidot et al. (2015) to find the optimal ensemble model optical property parameterization that best simulated globally measured infrared radiometric brightness temperatures. Furthermore, in this paper, the weights assigned to each of the ensemble members at each F07 PSD bin size are the same as those assumed in experiment 4 of B014b (i.e. Eq. (9) in that paper), which were 0.50, 0.20 and 0.30, respectively. This assignment of weights to the ensemble model is different from that found by Vidot et al. (2015) to achieve radiometric equivalence between the model and measurements. However, experiment 4 of B014b gave the best comparisons between the climate model runs and space-based shortwave and longwave radiation measurements. In contrast, the Vidot et al. (2015) analysis is based on measurements obtained at three wavelengths in the infrared. It is yet to be seen whether the weightings found in that paper would remain the same if more solar and infrared wavelengths were to be utilized. This will be the subject of a future paper; thus, we assume the same weightings as those used in experiment 4 of B014b.

In the MetUM configuration of models, atmospheric particulates such as aerosol, ice and water clouds are represented by vertical profiles of their mixing ratios with respect to air. In this paper and in B014b, the IWC becomes the ice mass mixing ratio, q_i , that is, the ratio between ice mass per unit volume and the mass of cloudy air per unit volume, and is in units of kg kg^{-1} . Likewise, the bulk optical properties, the volume extinction, and scattering coefficients become the mass extinction, K_{ext} , and mass scattering coefficients, K_{sca} , and both are in units of $\text{m}^2 \text{kg}^{-1}$ (i.e. the extinction and scattering coefficients per unit mass of cloudy air).

In this paper, the bulk optical property database is first divided into the six shortwave

and nine longwave Edwards–Slingo (1996, hereafter referred to as ES96) bands; these bands are defined in Table 1. In each of the ES96 bands, a total of about 10000 q_i and T_c values were randomly selected from the bulk optical property database of B014a. Selected values of q_i and T_c were between 1.0×10^{-8} and 0.004 kg kg^{-1} and -80°C and 0°C , respectively. This randomly selected range in q_i – T_c space is sufficient to capture the full range that might be generated in an atmospheric model. In each of the ES96 bands, the bulk optical properties were parameterized as nonlinear and linear functions, dependent on q_i and T_c , by an iterative minimization procedure. That is, the forms of the parameterizations were first assumed and then the coefficients, for each of the parameterizations, were estimated by iterating through possible coefficient values. This was done until differences between the parameterizations and randomly selected 10000 bulk optical properties were within acceptable experimental limits (i.e. estimated K_{ext} and K_{sca} values must be within $\pm 50\%$ of their true values for $> 90\%$ of all possible q_i – T_c values). The error of $\pm 50\%$ in the mass coefficients is based on likely in-situ errors in extinction estimates previously discussed in Baran et al. (2009). The errors resulting from this fitting procedure are discussed further below. The above fitting procedure resulted in the following best-fit bulk optical property parameterizations of cirrus:

$$K_{\text{ext}}(\lambda, q_i, T_c) = a_\lambda (q_i / T_c^4) \quad (2)$$

$$\omega_0(\lambda, q_i, T_c) = b_\lambda + c_\lambda q_i T_c \quad (3)$$

$$g(\lambda, q_i, T_c) = d_\lambda + e_\lambda q_i T_c \quad (4)$$

where the temperature, T_c , is in units of Kelvin. The ES96 estimated band-dependent coefficients a_λ , b_λ , c_λ , d_λ and e_λ are listed in Table 1. It should be noted that to obtain the correct asymptotic behavior for $\omega_0(\lambda, q_i, T_c)$ and $g(\lambda, q_i, T_c)$, for the cases where $q_i >$

1 $10^{-3} \text{ kg kg}^{-1}$, the values of ω_0 and g should assume the same values as ω_0 and g when
2 $q_i = 10^{-3} \text{ kg kg}^{-1}$. If this condition is applied, ω_0 and g should never attain unphysical
3 values. In B014b the above bulk optical properties are expressed as functions of q_i
4 only (i.e. Eqs. 4–7 in that paper). This is possible to do, as shown by Fig. 2, and is
5 equivalent to the parameterization proposed by McFarquhar et al. (2003). In that
6 paper, as previously stated, the IWC is explicitly derived as a function of r_{eff} ; in turn,
7 the bulk optical properties are derived as a function of r_{eff} . Thus, r_{eff} can be eliminated
8 between relationships to leave the bulk optical properties expressed as a function of
9 IWC only, which is equivalent to B014b.

10 The difference between the above parameterization and that of B014b is
11 highlighted by the following example. If we assume that $T_c = 190 \text{ K}$ and $q_i = 1.0 \times 10^{-3}$
12 kg kg^{-1} , Eq. (3) at ES96 shortwave band 5 (1.19–2.38 μm) gives $\omega_0 = 0.9015$, whilst
13 Eq. (6) from B014b gives $\omega_0 = 0.8663$. The former calculation is about 5% greater
14 than the latter calculation, which means that in the former case the cirrus is about
15 27% less absorbing (i.e., $\sim 1 - \omega_0$) than in the latter case. With such a difference in
16 shortwave absorption between the two parameterizations, the B014b parameterization
17 is clearly more likely to result in an increase in TTL temperature than Eq. (3).

18 In the introduction to this paper, it was noted that trigonal ice crystals were
19 observed by a number of studies in the TTL. Single-scattering calculations based on
20 trigonal ice crystals using the anomalous diffraction approximation (ADT) have been
21 reported by Murray et al. (2015). These calculations show that ω_0 , computed
22 assuming trigonal columns can be as much as 20% higher than their equivalent
23 hexagonal column counterparts for a range of crystal sizes they considered at an

absorbing wavelength. If the TTL were composed mostly of trigonal columns, then this would imply less solar absorption and, as a consequence, less in-cloud heating, due to generally larger ω_0 values, relative to Eq. (3). However, ADT is a soft particle approximation (i.e. assumes real refractive indices near unity), originally due to van de Hulst (1957), and so by using this approximation, ω_0 values presented in Murray et al. (2015) may be overestimated (due to the neglect of reflection; refraction and particle edge effects, which all tend to increase absorption, see for instance, Mitchell et al. 2006). The latter limitations of ADT were noted by Murray et al. (2015), who also called for more accurate computations of the single-scattering properties of trigonal particles. On the other hand, if the TTL were composed of quasi-spherical particles as reported in some studies cited in the introduction to this paper, the calculated ω_0 values of these particles would tend to be lower (due to geometrical considerations and edge effects, see Baran and Havemann 1999; Mitchell et al. 2006; Bi and Yang, 2014) than that calculated for the equivalent trigonal particles. This implies more absorption, and so, greater in-cloud heating in the TTL, assuming equal microphysics assumptions. This range in potential TTL in-cloud heating is indicative of the current uncertainties in the microphysics composition within the TTL. Reducing uncertainty in calculated ω_0 values requires observations of PSDs, ice particle shapes, and application of electromagnetic methods and not gross approximations such as ADT to observed TTL microphysics measurements.

The accuracy of the new parameterizations was tested by selecting an independent set of about 10000 q_i and T_c values taken from the ice optical property database of B014a. As before, the bulk optical properties, as a function of q_i and T_c , are grouped

into their ES96 bands. The test of accuracy of the new parameterizations is based on the relative percent error, $\varepsilon(\lambda)$, which given by:

$$\varepsilon_{\lambda} = \frac{\text{true}_{\lambda} - \text{estimated}_{\lambda}}{\text{true}_{\lambda}} \times 100\% \quad (5)$$

where in Eq. (5) true_{λ} and $\text{estimated}_{\lambda}$ are the actual bulk optical properties in the B014b database consisting of 2.986×10^6 values (i.e. 20662 q_i - T_c values \times 145 wavelengths – 10000 randomly selected values) and the estimated values using Eqs. (2–4), respectively. Here, the accuracy of the parameterizations is illustrated using only ES96 shortwave band 5 (1.19–2.38 μm), as all other bands have similar accuracies, and this band is important for the shortwave heating of cirrus in the TTL.

The calculated normalized PDFs of $\varepsilon(\lambda)$ are shown for $K_{\text{ext}}(\lambda, q_i, T_c)$, $K_{\text{sca}}(\lambda, q_i, T_c)$ and g in Figs. 4a–c, respectively. Figs. 4a and b show that $\varepsilon(\lambda)$ in the mass parameterizations is within $\pm 50\%$ for about 90% and 94% of the independently selected database, respectively. Typically, the in-situ measurement error in $K_{\text{ext}}(\lambda, q_i, T_c)$ is usually $\pm 50\%$ (Baran et al. 2009), so the relative error distribution shown in Figs. 4a–b is acceptable. Fig. 4c shows $\varepsilon(\lambda)$ for g and, as can be seen from the figure, $\varepsilon(\lambda)$ is within $\pm 2.5\%$ for about 83% of the database, which is also acceptable. Theoretical and in-situ uncertainty in the asymmetry parameter value is far greater than the error in the g parameterization (Ulanowski et al. 2006; Fu 2007; Garrett 2008; Baran 2012; van Diedenhoven et al. 2014). We compare our parameterization of g to the g parameterization developed by Fu (2007) by assuming q_i and T_c values of $1.0 \times 10^{-4} \text{ kg kg}^{-1}$ and 190 K, respectively. In Fu (2007), g is parameterized in the shortwave by assuming hexagonal columns and hexagonal plates

1 as a function of an effective AR by using either rough or smooth collections of
 2 particles. The range in the effective aspect ratio given by Fu (2007) represents the
 3 aspect ratios of monomer ice crystals that make up more complex ice crystals. Indeed,
 4 the effective AR of the ensemble model members assumed in this paper are 1.0, 0.42
 5 and 0.42 (the first being the hexagonal ice column of AR=1.0, and the latter two
 6 being the AR and averaged AR values found for the six-branched bullet rosette and
 7 the three monomer hexagonal ice aggregate, respectively), and the following weights
 8 of 0.50, 0.20 and 0.30 are assigned to the three ensemble members, respectively. The
 9 comparison is made by using the coefficients d_λ and e_λ tabulated in Table 1 at ES96
 10 shortwave band 1 (i.e. 0.20–0.32 μm) and at ES96 shortwave band 3 (0.32–0.69 μm).
 11 These two shortwave bands cover the wavelength range given in Fu (2007), for
 12 shortwave band 1 (i.e. 0.25–0.70 μm) given in that paper. Although the comparison is
 13 not exact in terms of the wavelength range and assumed ice microphysics, it is
 14 considered sufficiently accurate for the purposes of this paper. Applying the above
 15 three effective AR ratios for each of the ensemble models to Eqs. (3.2 and 2.2) given
 16 in Fu (2007), and weighting the calculated asymmetry parameter values by the three
 17 weights given above, we find a weighted value of 0.765 for g (i.e.
 18 $0.5 \times 0.73 + 0.20 \times 0.80 + 0.3 \times 0.80$). This Fu (2007) asymmetry parameter value
 19 compares to the values of 0.757 and 0.787 found for ES96 shortwave bands 1 and 3,
 20 respectively, and the average of these two values is 0.772. The averaged value is
 21 within about 1% of the Fu (2007) calculation, and the values calculated at the two
 22 ES96 shortwave bands are within about $\pm 2\%$ of Fu (2007). If we take $g=0.765$ and
 23 $g=0.787$ (i.e. the most extreme difference) and assume that the cirrus is located over a

1 dark ocean and conservative scattering, then the backward solar reflection is about
2 23.5 and 21.3%, respectively, where backward reflection $\sim (1.-g)$. The difference in
3 reflected shortwave flux is at most about 7 Wm^{-2} , assuming an area-averaged incident
4 solar flux of 330 Wm^{-2} , at least for the case considered here. These differences found
5 for the g parameterizations are far less than the range in g found by the following
6 studies (Ulanowski et al. 2006; Fu 2007; Garrett 2008; Baran 2012; van Diedenhoven
7 et al. 2014, Yang et al. 2015). Indeed, in the case of Ulanowski et al. (2006),
8 experimentally derived g values were found to vary between 0.80 ± 0.04 and 0.63 ± 0.05
9 for smooth and rough ice analog rosettes, respectively, and this difference results in a
10 shortwave flux uncertainty of about -56 Wm^{-2} . Furthermore, the calculated
11 asymmetry parameter values using the two parameterizations compare well against
12 radiometrically derived asymmetry parameter values using POLDER observations
13 from van Diedenhoven et al. (2014). The observations from POLDER were located
14 over the north coast of Australia. In that paper, at a T_c value of about -85°C , the
15 asymmetry parameter values are shown to vary between about 0.74 ± 0.02 and
16 0.79 ± 0.04 , which encompass the values of g , derived using the two completely
17 different parameterizations. These experimental results obtained at $0.865 \mu\text{m}$, were
18 roughly coincident with the three assumed shortwave bands used in the comparisons,
19 and the imaginary index of ice is very weakly absorbing at all of the chosen
20 shortwave bands as shown in B014b. At least at TTL temperatures, the parameterized
21 g values derived in this paper appear representative of other independent derivations
22 of g . However, g is one of the bulk ice optical properties that is important to constrain
23 in climate models, as noted by Stephens et al. (1990). In this paper, we are concerned

about TTL heating and specific humidity errors in a climate model, and these errors are more associated with the parameterizations found for $K_{\text{ext}}(\lambda, q_i, T_c)$ and $\omega_0(\lambda, q_i, T_c)$.

Eqs. (2) and (3) are now compared against the equivalent parameterizations developed by B014b. The parameterizations of g are not compared here as the results are not sufficiently different. In comparing the parameterizations a constant value of q_i is assumed, with its value being $1.0 \times 10^{-5} \text{ kg kg}^{-1}$, whilst the temperature is allowed to vary between -80°C and 0°C . The comparisons are shown in Figs. 5a–c at ES96 shortwave band 5 for $K_{\text{ext}}(\lambda, q_i, T_c)$, the co-albedo (i.e., $1 - \omega_0(\lambda, q_i, T_c)$), and (c) $K_{\text{abs}}(\lambda, q_i, T_c)$ (i.e., $K_{\text{abs}}(\lambda, q_i, T_c) = K_{\text{ext}}(\lambda, q_i, T_c) - K_{\text{sca}}(\lambda, q_i, T_c)$), respectively. Other bands show generally similar results to Figs. 5a–c and are not shown here for reasons of brevity. Fig. 5a shows that at T_c values of about -80°C , the nonlinear parameterization of $K_{\text{ext}}(\lambda, q_i, T_c)$ is about a factor of 2.5 greater than that predicted by B014b. This means that at typical TTL temperatures, the new parameterization, relative to B014b, will transmit less longwave terrestrial radiation to space through the cirrus, which will result in less longwave absorption by trace gases above the TTL cirrus, consequently lowering TTL temperatures through emission at cold temperatures. Also critical to the TTL temperature is the co-albedo. The co-albedo comparisons are shown in Fig. 5b; again, the figure shows that at $T_c = -80^\circ\text{C}$, the new parameterization co-albedo is less than B014b by almost a factor of 7. This change in absorption between the parameterizations is shown clearly in Fig. 5c, which shows $K_{\text{abs}}(\lambda, q_i, T_c)$, and at $T_c = -80^\circ\text{C}$, the new parameterization is almost a factor 3 times less absorbing than B014b. The comparisons show that the temperature-dependent parameterization in the TTL should result in less cirrus heating relative to B014b. The next section presents the impact of these different heating profiles on the

simulation of the TTL in an atmosphere-only climate integration using the MetUM.

3. The impact of the parameterizations on the simulation of the TTL

To assess the fidelity of the TTL simulation in models using the B014b parametrization and the parametrization described in section 2, we perform a pair of 20-year atmosphere-only climate simulations using each parametrisation. Apart from the formulation of the ice cloud optical properties, these simulations each use an identical baseline of the Global Atmosphere 6.0 (GA6.0) configuration of the MetUM. GA6.0 is described by Walters et al. (2015), so a description is not repeated here. The simulations are performed at a horizontal resolution of N96 (~135 km in the mid-latitudes) and use a vertical level set with spacings of between 500 and 700 m in the TTL region with a model “lid” at 85 km from the surface. The simulations run from December 1988 to November 2008 and use prescribed (but time-varying) sea-surface temperatures, greenhouse gas concentrations, and aerosol emissions while roughly following the protocol of the Atmospheric Model Intercomparison Project (AMIP, Taylor et al. 2012). Results are presented for the meteorological season December–January–February (DJF), as this season represents the period during which cirrus occurrence in the tropics is at a maximum (Sassen et al. 2008). The climate model predictions are compared against the ERA-Interim reanalysis temperature product (Dee et al. 2011) and the Modern-ERA Retrospective analysis for Research and Applications (MERRA) specific humidity product (Rienecker et al. 2011). The impacts of the parameterizations on the 20-year averaged DJF cloudy shortwave and longwave radiative effects at TOA are compared against the Loeb et al. (2009) reanalysis of the Clouds and the Earth’s Radiant Energy System (CERES) product.

1 Firstly, the DJF zonally averaged temperature differences between the B014b
2 parameterization and the ERA-Interim reanalysis are shown in Fig. 6a, whilst the same
3 differences are shown in Fig. 6b but for the new parameterizations. It is clear from Fig.
4 6b, relative to Fig. 6a, that the new parameterizations have reduced the TTL temperature
5 by about 1 K, and generally throughout the tropics, which is consistent with the
6 discussion surrounding Figs. 5a and b. In addition, the new parameterization has also
7 removed the warming in the southern sub-tropical troposphere region by about 1–2 K,
8 and reduced cooling and warming over the South and North Poles, respectively. On the
9 negative side, the new parameterizations lead to a cooling of the tropical troposphere by
10 about 1 K, and to a similar cooling at altitudes between about 15 and 30 hPa, which
11 occurs near the equator.

12 The impact of the new parameterizations on the model bias of zonally averaged
13 \log_{10} (specific humidity), relative to MERRA, is shown in Fig. 6d. The figures show that
14 the impact of the new parameterizations on the \log_{10} (specific humidity) model bias in the
15 TTL is to reduce it, and its distribution throughout the TTL, especially around the
16 equatorial region. Relative to the B014b parameterization, shown in Fig. 6c, the new
17 parameterization reduces the \log_{10} (specific humidity) model bias in the TTL by about 0.1
18 $\log_{10}(\text{kg kg}^{-1})$ and generally reduces the extent of this bias in the sub-tropics. For each
19 panel shown in Figs. 6a–d, the grid point root mean square errors (RMS) were calculated
20 over the region between 20°S and 20°N, and between 150 and 70 hPa. The resulting RMS
21 errors were found to be 2.52, 1.90 K, and 0.13 and 0.12 $\log_{10}(\text{kg kg}^{-1})$, respectively.
22 Therefore, in the TTL region, the new parameterization reduces the zonally averaged
23 temperature and specific humidity biases in the model.

1 Finally, to show that the new parameterizations do not result in any detriment to the
2 climate model, in terms of the cloud radiative effect at TOA and global means. Results
3 are presented for the model's predicted radiative effects in Figs. 7a–d and global means
4 in Table 2. The figures show that the new parameterization improves the shortwave and
5 longwave cloud radiative effects in the climate model, relative to B014b. The extent of
6 the shortwave bias in the model is significantly reduced, as shown by the reduction in the
7 area-weighted RMS error by 1.08 Wm^{-2} , and this improvement is especially evident in the
8 tropics. Note also the reduction in bias brought about by the new parameterization
9 throughout the Southern Ocean. The longwave biases in the climate model are also
10 reduced by the new parameterizations as shown in Figs. 7c and 7d, where it can be seen
11 that the area-averaged RMS error is reduced by 0.41 Wm^{-2} . The significant longwave
12 negative biases around the warm pool shown in Fig. 7c have been reduced by the new
13 parameterizations by up to about 20 Wm^{-2} , as demonstrated by Fig. 7d.

14 Table 2 shows a comparison between the Stephens et al. (2012) estimated CERES
15 global means for seven variables together with their estimated standard deviation $\pm\sigma$, and
16 the B014b and temperature-dependent parameterizations. The table shows that the
17 temperature-dependent parameterization is within the estimated uncertainty for six out of
18 seven of the global mean variables shown in table 2. This improves on the B014b
19 parameterization, which has four out of seven variables within the estimated uncertainty.
20 In particular, the B014b parameterization significantly underestimates the reflected
21 shortwave flux at TOA. As a result of this underestimation, the predicted shortwave
22 radiative effect is too low relative to the CERES estimated mean. The temperature-
23 dependent parameterization does predict adequate reflected shortwave flux at TOA, but

the prediction of the shortwave radiative effect is just over 1σ from the CERES estimated mean. This compares to about $1\frac{3}{4}\sigma$ from the estimated mean found for the B014b parameterization. The reason for this discrepancy between the parameterizations and the CERES observations for this variable is probably due to, in the case of B014b; the mass extinction coefficient being underestimated at about temperatures $< -40^{\circ}\text{C}$, as can be seen from Fig. 5a, relative to the temperature-dependent parameterization. In the case of the temperature-dependent parameterization, the physical reasons for this underestimation could be due to: (i) There is too little ice mass being predicted by the model cloud scheme and/or (ii) the model asymmetry parameter is too large. It is yet to be seen which of these reasons might account for the discrepancy in the shortwave radiative effect. However, in general, the new parameterization presented within this paper improves the model performance, relative to B014b, in terms of the shortwave and longwave cloudy radiative effect as can be seen from Figs. 7b–d, but also the predictions of model global mean fluxes.

4. Conclusions

A cirrus bulk optical property parameterization has been presented, and it has been demonstrated that the parameterization reduces zonally averaged temperature biases in the TTL of GA 6.0 by about 1–2 K relative to the B014b parameterizations. The parameterization of the asymmetry parameter was compared against an independent parameterization and was shown to be within about 1% and $\pm 2\%$ of the latter parameterization at ES96 short wavebands 1 and 2, respectively. Moreover, the asymmetry parameters predicted by both parameterizations were shown to encompass space-based estimations of g from observations from around the north coast of Australia

1 at TTL cirrus temperatures of -85°C . The reason for this improvement in climate model
2 performance is through coupling the bulk optical properties to q_i and T_c . At the low
3 temperatures in the TTL, the B014b parameterization will under-predict the single-
4 scattering albedo, resulting in TTL warming due, in part, to the absorption of shortwave
5 radiation, highlighting the importance of wavelengths in the near-infrared. The new
6 temperature-dependent parameterization also improves, relative to B014b, on
7 representing the model's prediction of the shortwave and longwave cloudy radiative
8 effect as well as global flux means. To improve climate model representations of the
9 TTL, more careful consideration should be given to the calculation of ice optical
10 properties, especially the mass extinction coefficients and single-scattering albedo, which
11 are the bulk ice optical properties that principally determine the temperature and specific
12 humidity distributions in our simulations of TTL cirrus. Further observations of cirrus
13 PSDs, IWCs, habits (in addition to humidity and temperature measurements), and solar
14 and infrared radiative properties in the TTL should be considered a priority.

15 **Acknowledgements**

16 The work of Steven C. Hardiman was supported by the joint DECC/Defra Met Office
17 Hadley Centre Climate Programme (GA01101). Three reviewers are thanked for their
18 contributions to this paper.

REFERENCES

- Baran, A. J., and S. Havemann, 1999: Rapid computation of the optical properties of hexagonal columns using complex angular momentum theory, *J. Quant. Spectrosc. Radiat. Transf.*, **63**, 499–519.
- Baran, A. J, and L.-C. Labonnote, 2007: A self-consistent scattering model for cirrus. 1: The solar Region. *Q. J. R. Meteorol. Soc.* **133**, 1899-18912, doi:10.1002/qj.164.
- Baran, A. J., 2009: A review of the light scattering properties of cirrus. *J. Quant. Spectrosc. Radiat. Transf.*, **110**, 1239–1260, doi:10.1016/j.jqsrt.2009.02.026.
- Baran, A. J, P. J., Connolly, and C. Lee, C, 2009: Testing an ensemble model of cirrus ice crystals using mid-latitude in situ estimates of ice water content, volume extinction coefficient, and the total solar optical depth, *J. Quant. Spectrosc. Radiat. Transfer.*, **110**, 1579–1598, doi:10.1016/j.jqsrt.2009.02.021.
- Baran, A. J, A. Bodas-Salcedo, R. J. Cotton, C. Lee, 2011a: Simulating the equivalent radar reflectivity of cirrus at 94 GHz using an ensemble model of cirrus ice crystals: A test of the Met Office global numerical weather prediction model. *Q. J. R. Meteorol. Soc.* **137**, 1547–1560. doi: 10.1002/qj.870
- Baran, A. J., Connolly, P. J., Heymsfield, A. J. and Bansemer, A., 2011b: Using in situ estimates of ice water content, volume extinction coefficient, and the total solar optical depth obtained during the tropical ACTIVE campaign to test an ensemble model of cirrus ice crystals. *Q.J.R. Meteorol. Soc.*, **137**, 199–218. doi: 10.1002/qj.731

1 Baran, A. J, 2012: From the single-scattering properties of ice crystals to climate
2 prediction: A way forward. *Atmos. Res.*, **112**, 45-69,
3 doi:10.1016/j.atmosres.2012.04.010.

4 Baran, A. J., R. Cotton, K. Furtado, S. Havemann, L.-C. Labonnote, F. Marengo, A. J.
5 Smith, J.-C. Thelen, 2014a: A self-consistent scattering model for cirrus. Part II:
6 The high and low frequencies. *Q. J. R. Meteorol. Soc.*, **140**, 1039-1057,
7 doi:10.1002/qj.2193.

8 Baran, A. J., P. Hill, K. Furtado, P. Field, and J. Manners, 2014b: A coupled cloud
9 physics-radiation parameterization of the bulk optical properties of cirrus and its
10 impact on the Met Office Unified Model Global Atmosphere 5.0 Configuration. *J.*
11 *Climate*, **27**, 7725-7752. <http://dx.doi.org/10.1175/JCLI-D-13-00700.1>

12 Bi, L., and P. Yang, 2014: High-frequency extinction efficiencies of spheroids: rigorous
13 T-matrix solutions and semi-empirical approximations, *Opt. Express* **22**, 10270-
14 10293.

15 Corti, T., B. P. Luo, Q. Fu, H. Vömel, and T. Peter, 2006: The impact of cirrus clouds on
16 tropical troposphere-to-stratosphere transport, *Atmos. Chem. Phys.*, **6**, 2539-2547,
17 doi:10.5194/acp-6-2539-2006.

18 Cotton, R., S. Osborne, Z. Ulanowski, E. Hirst, P. H. Kaye, and R. S. Greenaway, 2010:
19 The Ability of the Small Ice Detector (SID-2) to Characterize Cloud Particle and
20 Aerosol Morphologies Obtained during Flights of the FAAM BAe-146 Research
21 Aircraft. *J. Atmos. Oceanic Technol.*, **27**, 290–303. doi:
22 <http://dx.doi.org/10.1175/2009JTECHA1282.1>.

Cotton, R. J., P. R. Field, Z. Ulanowski, P. H. Kaye, E. Hirst, R. S. Greenaway, I. Crawford, J. Crosier, and J. Dorsey, 2013: The effective density of small ice particles obtained from in situ aircraft observations of mid-latitude cirrus. *Q.J.R. Meteorol. Soc.*, **139**, 1923–1934. doi: 10.1002/qj.2058.

Dee, D. P., S. M. Uppala, A. J. Simmons, P. Berrisford, P. Poli, S. Kobayashi, U. Andrae, M. A. Balmaseda, G. Balsamo, P. Bauer, P. Bechtold, A. C. M. Beljaars, L. van de Berg, J. Bidlot, N. Bormann, C. Delsol, R. Dragani, M. Fuentes, A. J. Geer, L. Haimberger, S. B. Healy, H. Hersbach, E. V. Hólm, L. Isaksen, P. Kallberg, M. Köhler, M. Matricardi, A. P. McNally, B. M. Monge-Sanz, J-J Morcrette, B-K Park, C. Peubey, P. de Rosnay, C. Tavolato, J-N Thépaut, and F. Vitart, 2011: The ERA-Interim reanalysis: configuration and performance of the data assimilation system. *Q.J. R. Meteorol. Soc.*, **137**, 553–597, doi:10.1002/qj.828.

Delanoë, J., and R. J. Hogan, 2010: Combined CloudSat-CALIPSO-MODIS retrievals of the properties of ice clouds, *J. Geophys. Res.*, **115**, D00H29, doi:10.1029/2009JD012346.

Deng, M., G. G. Mace, Z. Wang, and H. Okamoto, 2010: Tropical Composition, Cloud and Climate Coupling Experiment validation for cirrus cloud profiling retrieval using CloudSat radar and CALIPSO lidar, *J. Geophys. Res.*, **115**, D00J15, doi:10.1029/2009JD013104.

Edwards, J. M. and A. Slingo, 1996: Studies with a flexible new radiation code, I: Choosing a configuration for a large-scale model. *Q. J. R. Meteorol. Soc.*, **122**, 689–719., doi:10.1002/qj.49712253107.

- 1 Edwards, J. M., S. Havemann, J.-C. Thelen, A. J. Baran, 2007: A new parameterization
2 for the radiative properties of ice crystals: Comparison with existing schemes and
3 impact in a GCM. *Atmos. Res.* **83**, 19–35, doi:10.1016/j.atmosres.2006.03.002.
- 4 Field, P. R., and A. J. Heymsfield, 2003: Aggregation and scaling of ice crystal size
5 distributions. *J. Atmos. Sci.*, 60, 544-560.
- 6 Field, P. R., A. J. Heymsfield, and A. Bansemer, 2006: Shattering and particle interarrival
7 times measured by optical array probes in ice clouds. *J. Atmos. Oceanic Technol.*,
8 23, 1357–1371, doi:10.1175/ JTECH1922.1.
- 9 Field, P. R., A. J. Heymsfield, and A. Bansemer, 2007: Snow size distribution
10 parameterization for midlatitude and tropical ice cloud. *J. Atmos. Sci.*, **64**, 4346-
11 4365, doi:10.1175/2007JAS2344.1.
- 12 Foot, J. S., 1988: Some observations of the optical properties of clouds. II: Cirrus. *Q.J.R.*
13 *Meteorol. Soc.*, **114**, 145–164, doi: 10.1002/qj.49711447908.
- 14 Fu, Q: 2007: A new parameterization of an asymmetry factor of cirrus clouds for climate
15 models, *J. Atmos. Sci.*, **64**, 4140-4150, doi:10.1175/2007JAS2289.1.
- 16 Furtado, K., P. R. Field, R. Cotton, A. J. Baran, 2015: The effects of ice particle fall
17 speed and size distribution on simulated high cloud. *Q.J.R. Meteorol. Soc.* 141,
18 1546-1559, doi: 10.1002/qj.2457.
- 19 Garrett, T., 2008: Observational quantification of the optical properties of cirrus cloud, in
20 *Light scattering Reviews 3*, edited by A. Kokhanovsky, Springer, 403pp.

1 Hardiman, S. C., I. A. Boutle, A. C. Bushell, N. Butchart, M. J. P. Cullen, P. R. Field, K.
 2 Furtado, J. C. Manners, S. F. Milton, C. Morcrette, F. M. O'Connor, B. J.
 3 Shipway, C. Smith, D. N. Walters, M. R. Willett, K. D. Williams, and N. Wood,
 4 2015: Processes controlling tropical tropopause temperature and stratospheric
 5 water vapor in climate models. *J. Climate*, **28**, 6516–6535. doi:
 6 <http://dx.doi.org/10.1175/JCLI-D-15-0075.1>
 7 Heymsfield, A. J., 1986: Ice particles observed in a cirriform cloud at -83°C and
 8 implications for polar stratospheric clouds. *J. Atmos. Sci.*, **43**, 851-855.
 9 Holz, R. E., S. Platnick, K. Meyer, M. Vaughan, A. Heidinger, P. Yang, G. Wind, S.
 10 Dutcher, S. Ackerman, N. Amarasinghe, F. Nagle, and C. Wang, 2015: Resolving
 11 ice cloud optical thickness biases between CALIOP and MODIS using infrared
 12 retrievals, *Atmos. Chem. Phys. Discuss.*, **15**, 29455-29495, doi:10.5194/acpd-15-
 13 29455-2015.
 14 Hong, Y., and G. Liu, 2015: The Characteristics of Ice Cloud Properties Derived from
 15 CloudSat and CALIPSO Measurements. *J. Climate*, **28**, 3880–3901.
 16 doi: <http://dx.doi.org/10.1175/JCLI-D-14-00666.1>.
 17 Houze, R. A., P. V. Hobbs, P. H. Herzegh, and D. B. Parsons, 1979: Size distributions of
 18 precipitation particles in frontal clouds. *J. Atmos. Sci.*, **36**, 156–162.
 19 Jensen, E. J., L. Pfister, T. V. Bui, P. Lawson, B. Baker, Q. Mo, D. Baumgardner, E. M.
 20 Weinstock, J. B. Smith, E. J. Moyer, T. F. Hanisco, D. S. Sayres, J. M. St. Clair,
 21 M. J. Alexander, O. B. Toon, and J. A. Smith, 2008: Formation of large (≈ 100
 22 μm) ice crystals near the tropical tropopause, *Atmos. Chem. Phys.*, **8**, 1621-1633,
 23 doi:10.5194/acp-8-1621-2008.

1 Jensen, E., L. Pfister, D. Jordan, T. Bui, R. Ueyama, H. Singh, T. Thornberry, A. Rollins,
 2 R. Gao, D. Fahey, K. Rosenlof, J. Elkins, G. Diskin, J. DiGangi, R. Lawson, S.
 3 Woods, E. Atlas, M. Navarro Rodriguez, S. Wofsy, J. Pittman, C. Bardeen, O.
 4 Toon, B. Kindel, P. Newman, M. McGill, D. Hlavka, L. Lait, M. Schoeberl, J.
 5 Bergman, H. Selkirk, M. Alexander, J. Kim, B. Lim, J. Stutz, and K. Pfeilsticker,
 6 2015: The NASA Airborne Tropical Tropopause EXperiment (ATTREX): High-
 7 Altitude Aircraft Measurements in the Tropical Western Pacific. *Bull. Amer.*
 8 *Meteor. Soc.* doi:10.1175/BAMS-D-14-00263.1, in press.

9 Korolev, A. V., E. F. Emery, J. W. Strapp, S. G. Cober, and G. A. Isaac, 2013:
 10 Quantification of the effects of shattering on airborne ice particle
 11 measurements. *J. Atmos. Oceanic Technol.*, 30, 2527–2553.

12 Lawson, R. P, B. Pilon, B. Baker, Q. Mo, E. Jensen, L. Pfister, and P. Bui, 2008:
 13 Aircraft measurements of microphysical properties of subvisible cirrus in the
 14 tropical tropopause layer, *Atmos. Chem. Phys.*, **8**, 1609-1620, doi:10.5194/acp-8-
 15 1609-2008.

16 Lee, J., P. Yang, A. E. Dessler, B-C. Gao, and S. Platnick, 2009: Distribution and
 17 Radiative Forcing of Tropical Thin Cirrus Clouds. *J. Atmos. Sci.*, **66**, 3721–3731.
 18 doi: <http://dx.doi.org/10.1175/2009JAS3183.1>.

19 Letu, H., H. Ishimoto, J. Riedi, T. Y. Nakajima, C.-L. Labonnote, A. J. Baran, T. M.
 20 Nagao, and M. Skiguchi, 2015: Investigation of ice particle habits to be used for
 21 ice cloud remote sensing for the GCOM-C satellite mission, *Atmos. Chem. Phys.*
 22 *Discuss.*, **15**, 31665-31703, doi:10.5194/acpd-15-31665-2015.

1 Liou, K. N, 1986: Influence of cirrus clouds on weather and climate processes: A global
2 perspective, *Mon. Weather Rev.*, **114**, 1167–1199, doi:10.1175/1520-
3 0493(1986)114<1167:IOCCOW>2.0.CO;2.

4 Liou, K. N, 2005: Cirrus clouds and climate, in McGraw-Hill 2005 Yearbook of Science
5 & Technology, pp. 51–53, McGraw Hill, Columbus, Ohio.

6 Loeb, N. G., B. A. Wielicki, D. R. Doelling, G. L. Smith, D. F. Keyes, S. Kato, N.
7 Manalo-Smith, and T. Wong, 2009: Toward Optimal Closure of the Earth's Top-
8 of-Atmosphere Radiation Budget. *J. Climate*, **22**, 748766,
9 doi10.1175/2008JCLI2637.1.

10 Mace, G. G., Q. Zhang, M. Vaughan, R. Marchand, G. Stephens, C. Trepte, and D.
11 Winker, 2009: A description of hydrometeor layer occurrence statistics derived
12 from the first year of merged Cloudsat and CALIPSO data, *J. Geophys. Res.*, **114**,
13 D00A26, doi:10.1029/2007JD009755.

14 McFarquhar, G. M., A. J. Heymsfield, J. Spinhirne, and B. Hart, 2000: Thin and
15 subvisual tropopause tropical cirrus: Observations and radiative impacts. *J.*
16 *Atmos. Sci.*, **57**, 1841–1853, doi:10.1175/1520-
17 0469(2000)057,1841:TASTTC.2.0.CO;2.

18 McFarquhar, G.M., S. Iacobellis, and R.C.J. Somerville, 2003: SCM simulations of
19 tropical ice clouds using observationally based parameterizations of microphysics.
20 *J. Climate*, **11**, 1643-1664.

21 Mitchell, D. L., A. J. Baran, W. P. Arnott, and C. Schmitt, 2006: Testing and comparing
22 the modified anomalous diffraction approximation. *J. Atmos. Sci.*, **63**, 2948–2962,
23 doi:10.1175/JAS3775.1

- 1 Mitchell, D.L., Rasch, P., Ivanova, D., McFarquar, G.M., Nousiainen, T., 2008:
2 Impact of small ice crystal assumptions on ice sedimentation rates in cirrus
3 clouds and GCM simulations. *Geophys. Res. Lett.* 35, L09806.
- 4 Murray, Benjamin J., Christoph G. Salzmänn, Andrew J. Heymsfield, Steven Dobbie,
5 Ryan R. Neely III, and Christopher J. Cox, 2015: Trigonal Ice Crystals in
6 Earth's Atmosphere. *Bull. Amer. Meteor. Soc.*, **96**, 1519–1531. doi:
7 <http://dx.doi.org/10.1175/BAMS-D-13-00128.1>
- 8 Rienecker, M. M., M. J. Suarez, R. Gelaro, R. Todling, J. Bacmeister, E. Liu, M. G.
9 Bosilovich, S. D. Schubert, L. Takacs, G-K. Kim, S. Bloom, J. Chen, D. Collins,
10 A. Conaty, A. da Silva, W. Gu, J. Joiner, R. D. Koster, R. Lucchesi, A. Molod, T.
11 Owens, S. Pawson, P. Pegion, C. R. Redder, R. Reichle, F. R. Robertson, A. G.
12 Ruddick, M. Sienkiewicz, and J. Woollen, 2011: MERRA: NASA's Modern-Era
13 Retrospective Analysis for Research and Applications. *J. Climate*, **24**, 3624–3648,
14 doi:<http://dx.doi.org/10.1175/JCLI-D-11-00015.1>.
- 15 Sassen, K., M. K. Griffin, and G. C. Dodd, 1989: Optical Scattering and Microphysical
16 Properties of Subvisual Cirrus Clouds, and Climatic Implications. *J. Appl.*
17 *Meteor.*, **28**, 91–98. doi: <http://dx.doi.org/10.1175/1520>
18 0450(1989)028<0091:OSAMPO>2.0.CO;2.
- 19 Sassen, K., and B. S. Cho, 1992: Subvisual-thin cirrus lidar dataset for satellite
20 verification and climatological research, *J. Appl. Meteorol.*, **31**, 1275–1285.

1 Sassen, K., Z. Wang, and D. Liu, 2008: Global distribution of cirrus clouds from
2 CloudSat/Cloud-Aerosol Lidar and Infrared Pathfinder Satellite Observations
3 (CALIPSO) measurements, *J. Geophys. Res.*, **113**, D00A12,
4 doi:10.1029/2008JD009972.

5 Schwartz, M. C., and G. G. Mace, 2010: Co-occurrence statistics of tropical tropopause
6 layer cirrus with lower cloud layers as derived from CloudSat and CALIPSO data.
7 *J. Geophys. Res.*, **115**, D20215, doi:10.1029/2009JD012778.

8 Sourdeval, O, C.-L. Labonnote, A. J. Baran and G. Brogniez, 2015: A methodology for
9 simultaneous retrieval of ice and liquid water cloud properties. Part I: Information
10 content and case study. *Q.J.R. Meteorol. Soc.*, **141**: 870–882. doi:
11 10.1002/qj.2405.

12 Stephens, G. L., S.-C. Tsay, P. W. Stackhouse Jr., and P. J. Flatau, 1990: The relevance
13 of the microphysical and radiative properties of cirrus clouds to climatic feedback.
14 *J. Atmos. Sci.*, **47**, 1742–1753.

15 Stephens, G. L., and Coauthors, 2012: An update on Earth’s energy balance in light of the
16 latest global observations. *Nature Geoscience*. 23rd September 2012. doi:
17 10.1038/NGEO1580

18 Stubenrauch C. J., F. Eddounia, J. M. Edwards, and A. Macke, 2007: Evaluation of
19 Cirrus Parameterizations for Radiative Flux Computations in Climate Models
20 Using TOVS–ScaRaB Satellite Observations. *J. Climate*, **20**, 4459–4475, doi:
21 <http://dx.doi.org/10.1175/JCLI4251.1>.

- 1 Taylor, J., W. Randel, and E.J. Jensen, 2011: Cirrus cloud-temperature interactions in the
2 tropical tropopause layer: A case study. *Atmospheric Chemistry and Physics*, **11**,
3 10085-10095, doi: 10.5194/acp-11-10085-2011.
- 4 Taylor, K. E., R. J. Stouffer, and G. A. Meehl, 2012: An Overview of CMIP5 and the
5 Experiment Design. *Bull. Amer. Meteor. Soc.*, **93**, 485–498, doi:
6 <http://dx.doi.org/10.1175/BAMS-D-11-00094.1>
- 7 Ulanowski, Z., E. Hesse, P. H. Kaye and A. J. Baran, 2006: Light scattering by complex
8 ice-analogue crystals. *J. Quantit. Spectr. Rad. Transf.* **100**, 382-92,
9 [doi:10.1016/j.jqsrt.2005.11.052](https://doi.org/10.1016/j.jqsrt.2005.11.052)
- 10 van de Hulst, H. C., 1957: Light Scattering by Small Particles. Wiley, 544 pp.
- 11 van Diedenhoven, B., A. M. Fridlind, B. Cairns, and A. S. Ackerman, 2014: Variation of
12 ice crystal size, shape, and asymmetry parameter in tops of tropical deep
13 convective clouds, *J. Geophys. Res. Atmos.*, **119**, 11,809–11,825,
14 [doi:10.1002/2014JD022385](https://doi.org/10.1002/2014JD022385).
- 15 Vidot, J., A. J. Baran, and P. Brunel, 2015: A new ice cloud parameterization for infrared
16 radiative transfer simulation of cloudy radiances: Evaluation and optimization
17 with IIR observations and ice cloud profile retrieval products. *J. Geophys. Res.*
18 *Atmos.*, **120**, 6937–6951. doi: 10.1002/2015JD023462.

Walters, D. N., M. E. Brooks, I. A. Boutle, T. R. O. Melvin, R. A. Stratton, A. C. Bushell, D. Copsey, P. E. Earnshaw, M. S. Gross, S. C. Hardiman, C. M. Harris, J. T. Heming, N. P. Klingaman, R. C. Levine, J. Manners, G. M. Martin, S. F. Milton, M. P. Mittermaier, C. J. Morcrette, T. C. Riddick, M. J. Roberts, P. M. Selwood, W. J. Tennant, P.-L. Vidale, J. M. Wilkinson, N. Wood, S. J. Woolnough, and P. K. Xavier, 2015: The Met Office Unified Model Global Atmosphere 6.0 and JULES Global Land 6.0 configurations, in preparation.

Wang, L. and A. E. Dessler, 2006: Instantaneous cloud overlap statistics in the tropical area revealed by ICESat/GLAS data, *Geophys. Res. Lett.*, **33**, L15804, doi:10.1029/2005GL024350.

Westbrook, C. D., R. C. Ball, P. R. Field, A. J. Heymsfield, 2004: Theory of growth by differential sedimentation, with application to snowflake formation, *Physical Review E - Statistical, Nonlinear, and Soft Matter Physics*, **70**, pp.021403-1-021403-7. doi: 10.1103/PhysRevE.70.021403.

Yang, P., K. N. Liou, L. Bi, C. Liu, B. Q. Yi, and B. A. Baum, 2015: On the radiative properties of ice clouds: Light scattering, remote sensing, and radiation parameterization, *Adv. Atmos. Sci.*, **32**, 32–63, doi:10.1007/s00376-014-0011-z.

Yang, Q., Q. Fu, and Y. Hu, 2010: Radiative impacts of clouds in the tropical tropopause layer, *J. Geophys. Res.*, **115**, D00H12, doi:10.1029/2009JD012393.

Yi, B., P. Yang, B. A. Baum, T. L’Ecuyer, L. Oreopoulos, E. J. Mlawer, A. J. Heymsfield, and K.-N. Liou, 2013: Influence of ice particle surface roughness on the global cloud radiative effect. *J. Atmos. Sci.*, **70**, 2794–2807, doi:10.1175/JAS-D-13-020.1.

1 Zhou, C., A. E. Dessler, M. D. Zelinka, P. Yang, and T. Wang, 2014: Cirrus feedback on
2 interannual climate fluctuations, *Geophys. Res. Lett.*, **41**,
3 doi:10.1002/2014GL062095.

1 Fig. 1. The bulk optical properties (a) ω_0 and (b) g as a function of the mass carrying
2 moment $M(2)$ and temperature at the wavelength of $1.575 \mu\text{m}$ for all 20662
3 values. The calculated values for ω_0 and g are shown as the color bar on the right-
4 hand side of the figures.

5 Fig. 2. The mass carrying moment $M(2)$ as a function of the mean effective dimension,
6 D_{eff} , and temperature, T_c , for all 20662 values. The key on the right-hand side of
7 the figure is T_c in units of $^{\circ}\text{C}$.

8 Fig. 3. The 20662 calculated values of ω_0 as a function of (a) D_{eff} and (b) $M3/M2$, the
9 mean mass-weighted size, D_{mmw} , of the PSD. The key on the right-hand side of
10 the figures is the calculated values of ω_0 at the wavelength of $1.575 \mu\text{m}$.

11 Fig. 4. The normalized PDFs of the relative percent error in the parameterization of (a)
12 $K_{\text{ext}}(\lambda, q_i, T_c)$, (b) $K_{\text{sca}}(\lambda, q_i, T_c)$, and (c) $g(\lambda, q_i, T_c)$. Relative percent error results
13 are shown for Edwards and Slingo (1996) shortwave band 5 ($1.19\text{--}2.38 \mu\text{m}$).

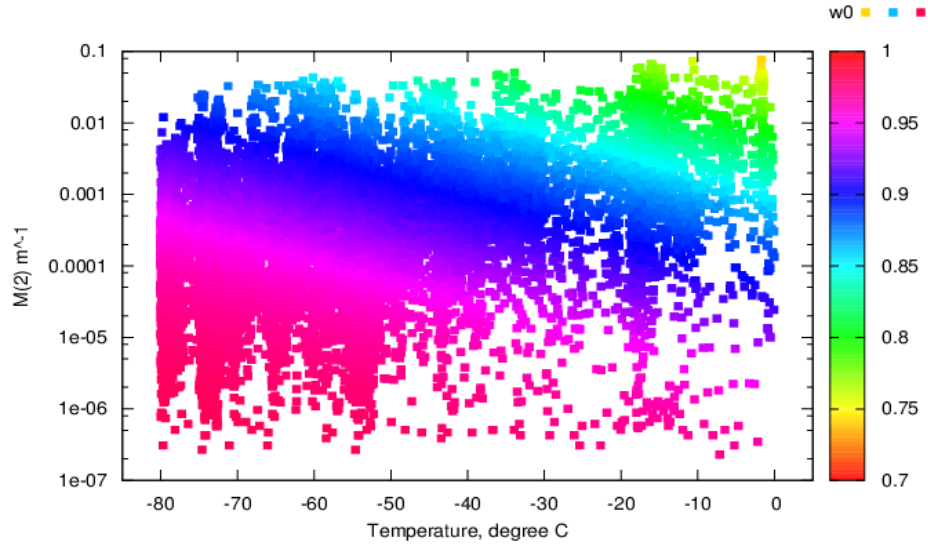
14 Fig. 5. Comparing the new parameterization (full line) to the B014b parameterization
15 (dashed line) at Edwards and Slingo (1996) shortwave band 5 ($1.19\text{--}2.38 \mu\text{m}$).
16 Comparisons are shown for (a) $K_{\text{ext}}(\lambda, q_i, T_c)$, (b) the co-albedo, and (c) $K_{\text{abs}}(\lambda, q_i,$
17 $T_c)$.

1 Fig. 6. The 20-year DJF zonally averaged temperature and log10 (specific humidity)
2 differences, shown in the top and bottom panels, respectively. The differences are
3 between the MetUM configuration 6.0 run, the ERA-Interim and MERRA
4 products, respectively. In the left column, panels (a) and (c), results are shown
5 while assuming the B014b parameterization. In the right column, panels (b) and
6 (d), results are shown while assuming the new parameterization. The units of
7 temperature difference and log (specific humidity) are K and log10 (kg kg⁻¹),
8 respectively.

9 Fig. 7. The annual 20-year TOA cloud radiative effect differences between MetUM
10 configuration 6.0 and the CERES products. Results are shown for the shortwave
11 while assuming the (a) B014b parameterization and (b) the new parameterization.
12 The longwave results are shown while assuming the (c) B014b parameterization
13 and (d) the new parameterization. The area-averaged root mean square difference
14 is shown in each of the panels, and differences are in units of Wm⁻².

1

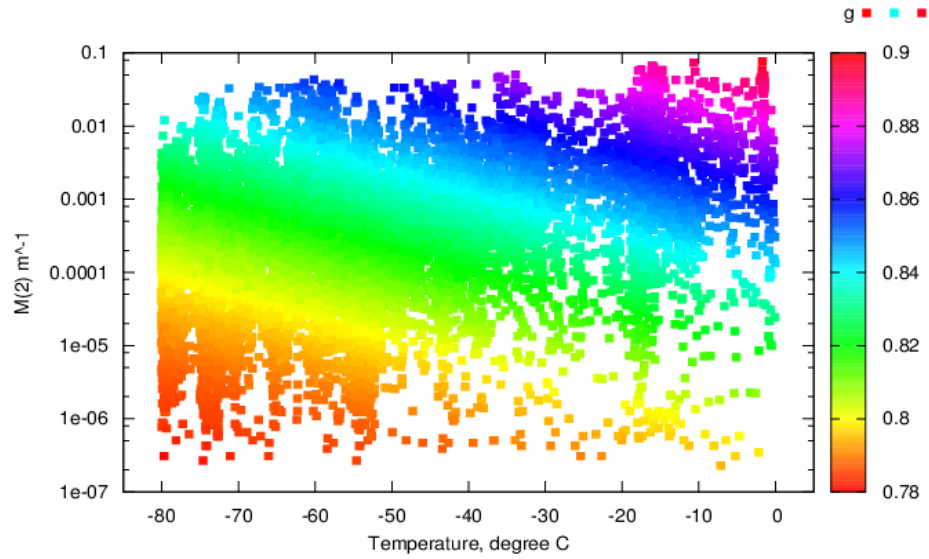
(a)



2

3

(b)



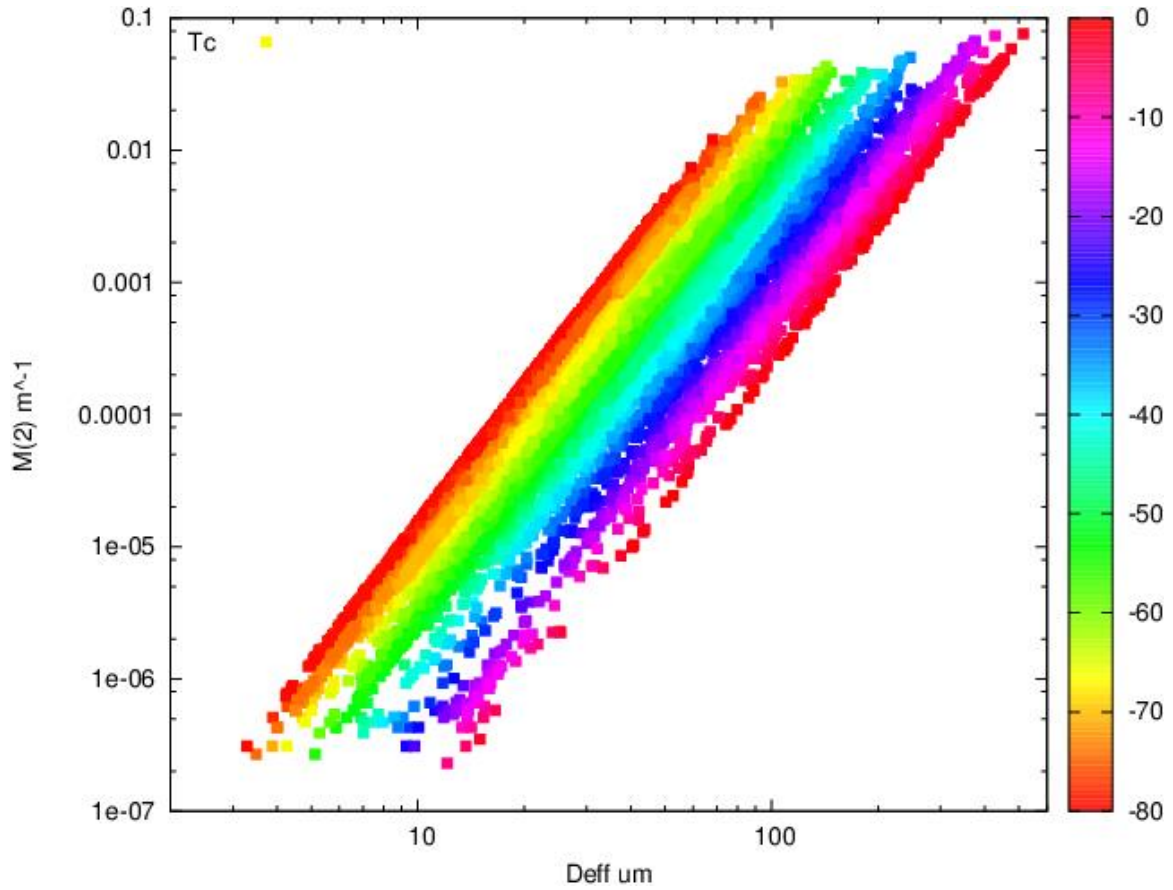
4

Fig. 1. The bulk optical properties (a) w_0 and (b) g as a function of the mass carrying moment $M(2)$ and temperature at the wavelength of $1.575 \mu\text{m}$ for all 20662 values. The calculated values for w_0 and g are shown as the color bar on the right-hand side of the figures.

9

10

1



2

3 Fig. 2. The mass carrying moment $M(2)$ as a function of the mean effective dimension,
 4 D_{eff} , and temperature, T_c , for all 20662 values. The key on the right-hand side of
 5 the figure is T_c in units of $^{\circ}\text{C}$.

6

7

8

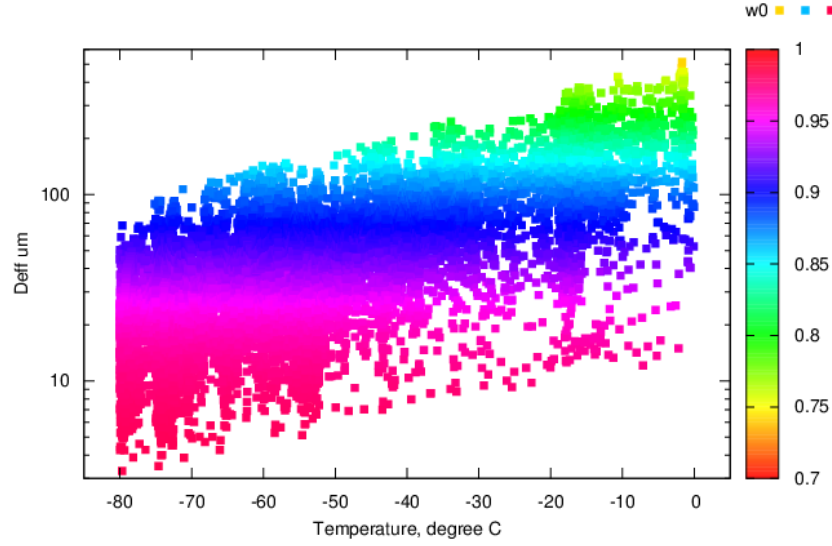
9

10

11

12

(a)



(b)

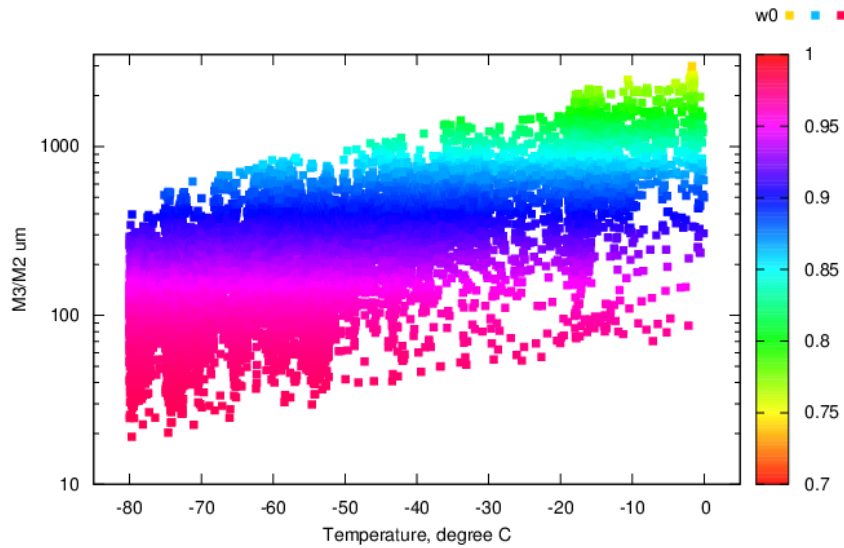


Fig. 3. The 20662 calculated values of w_0 as a function of (a) D_{eff} and (b) M_3/M_2 , the mean mass-weighted size, D_{mmw} , of the PSD. The key on the right-hand side of the figures is the calculated values of w_0 at the wavelength of $1.575 \mu\text{m}$.

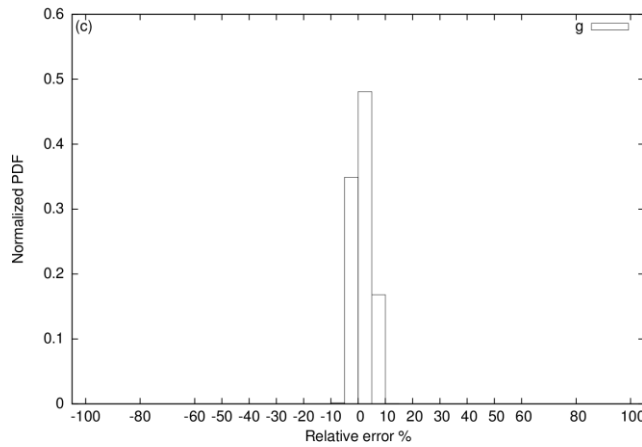
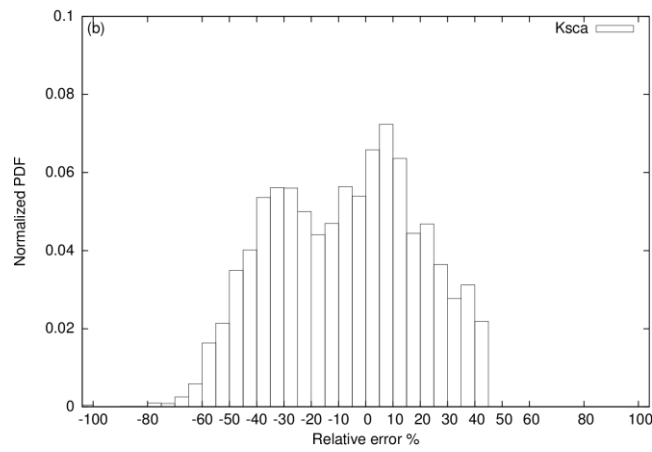
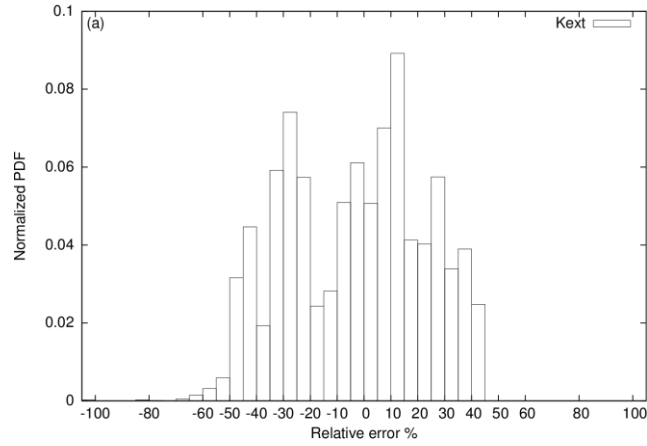


Fig. 4. The normalized PDFs of the relative percent error in the parameterization of (a) $K_{ext}(\lambda, q_i, T_c)$, (b) $K_{sca}(\lambda, q_i, T_c)$, and (c) $g(\lambda, q_i, T_c)$. Relative percent error results are shown for Edwards and Slingo (1996) shortwave band 5 (1.19–2.38 μm).

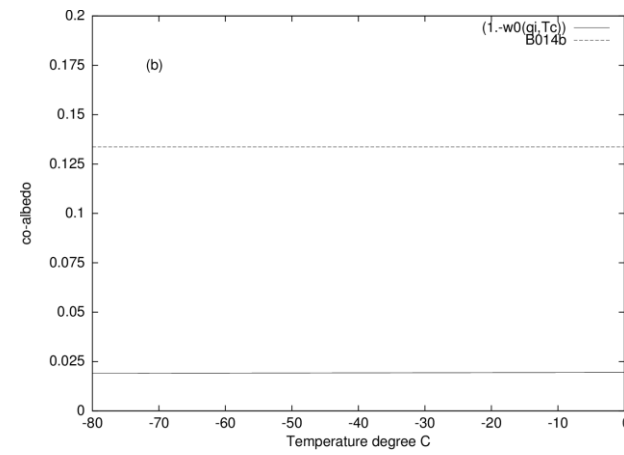
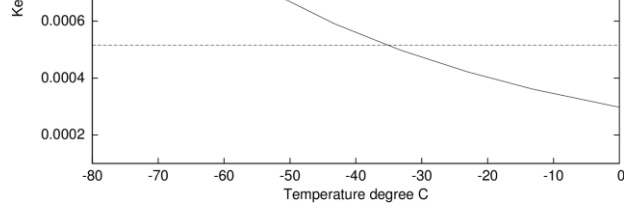
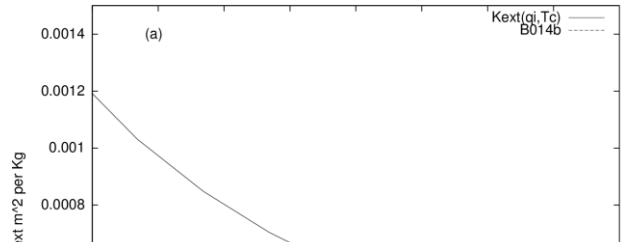
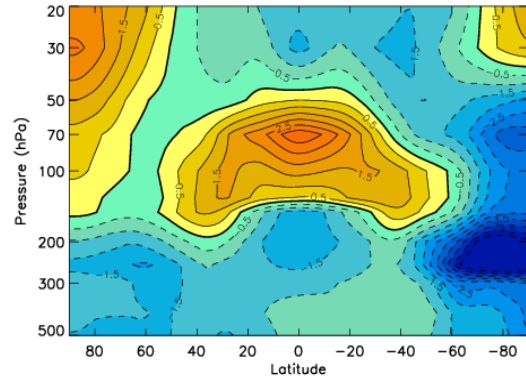
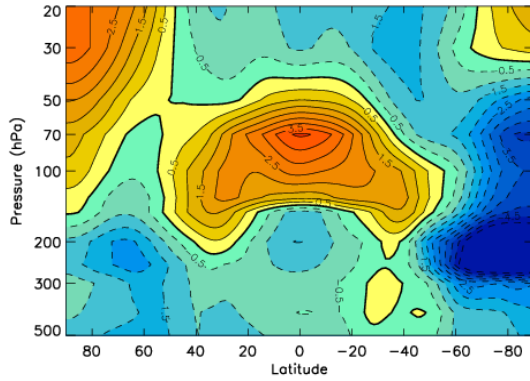


Fig. 5. Comparing the new parameterization (full line) to the B014b parameterization (dashed line) at Edwards and Slingo (1996) shortwave band 5 (1.19–2.38 μm). Comparisons are shown for (a) $K_{\text{ext}}(\lambda, q_i, T_c)$, (b) the co-albedo, $(1.-\omega_0(\lambda, q_i, T_c))$, and (c) $K_{\text{abs}}(\lambda, q_i, T_c)$.

1

(a)

(b)

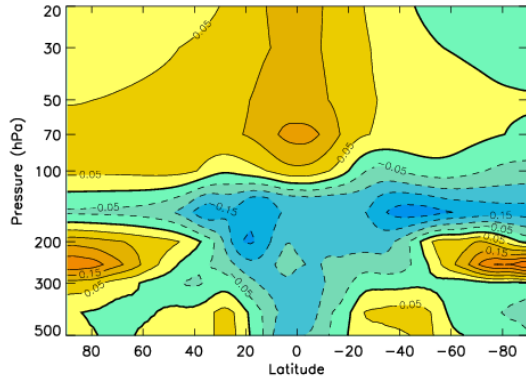
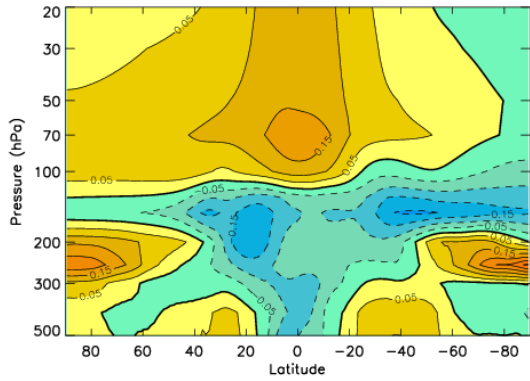


2

3

(c)

(d)



4

5 Fig. 6. The 20-year DJF zonally averaged temperature and log10 (specific humidity)

6 differences, shown in the top and bottom panels, respectively. The differences are

7 between the MetUM configuration 6.0 run, the ERA-Interim and MERRA

8 products, respectively. In the left column, panels (a) and (c), results are shown

9 while assuming the B014b parameterization. In the right column, panels (b) and

10 (d), results are shown while assuming the new parameterization. The units of

11 temperature difference and log (specific humidity) are K and log10 (kg kg⁻¹),

12 respectively.

13

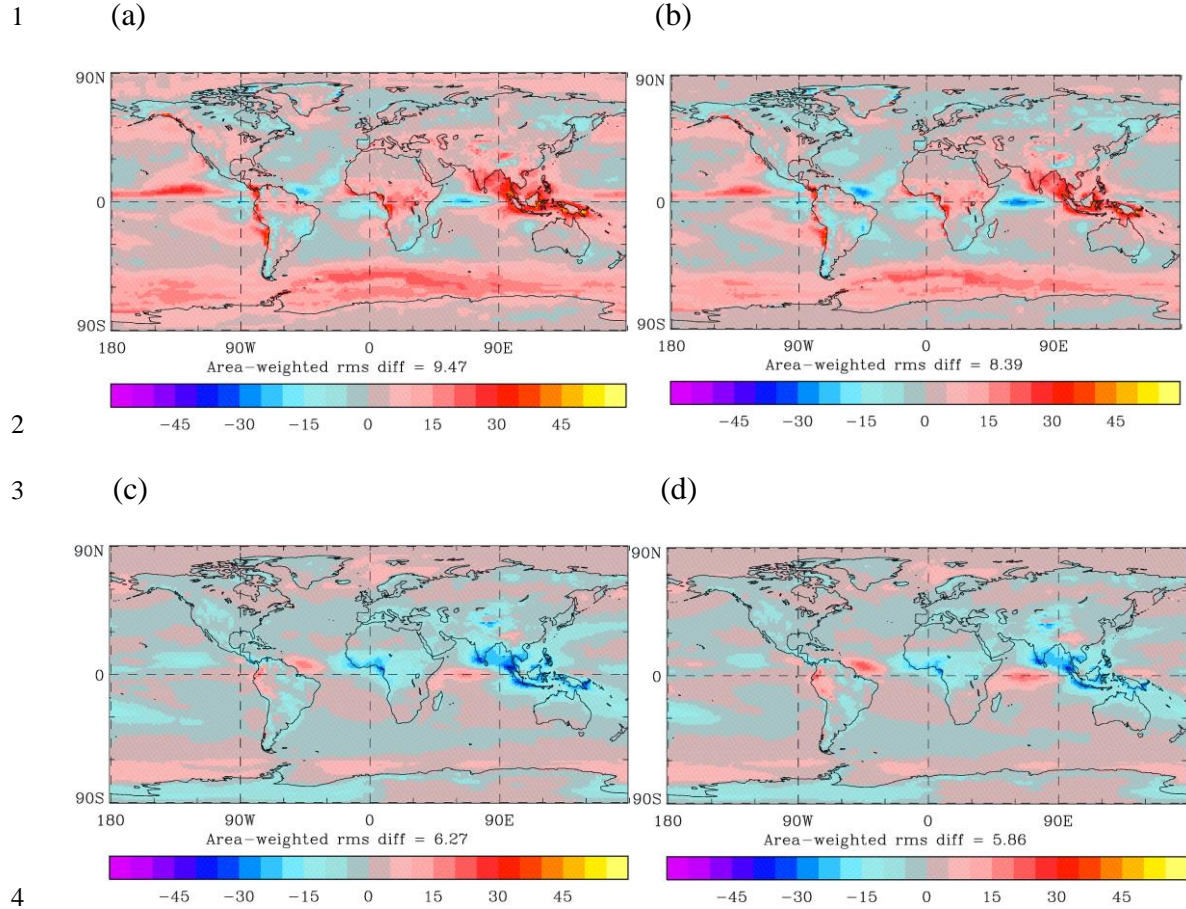


Fig. 7. The annual 20-year TOA cloud radiative effect differences between MetUM configuration 6.0 and the CERES products. Results are shown for the shortwave while assuming the (a) B014b parameterization and (b) the new parameterization. The longwave results are shown while assuming the (c) B014b parameterization and (d) the new parameterization. The area-averaged root mean square difference is shown in each of the panels, and differences are in units of Wm^{-2} .

- 1 Table 1. The derived values of the band-dependent coefficients for each of the
- 2 Edwards and Slingo (1996) shortwave and longwave bands. The first six entries in the
- 3 table are the shortwave bands and the following nine entries are the longwave bands.

Band μm	a_λ	b_λ	c_λ	d_λ	e_λ
0.20–0.32	1.64×10^{11}	1.0000	6.5×10^{-15}	0.7560	0.0378
0.32–0.69	1.66×10^{11}	1.0000	-1.4×10^{-6}	0.7804	0.0419
0.32–0.69	1.64×10^{11}	0.9999	-6.4×10^{-5}	0.7860	0.0434
0.69–1.19	1.64×10^{11}	0.9996	-0.0031	0.7897	0.0468
1.19–2.38	1.65×10^{11}	0.9817	-0.4218	0.8208	0.1351
2.38–10.0	1.60×10^{11}	0.7500	-0.2353	0.9130	0.1240
25.0– 10^4	1.50×10^{11}	0.6300	-0.2500	0.7129	0.6568
18.18–25.0	1.75×10^{11}	0.7700	-0.2866	0.8356	0.3085
12.50– 18.18	1.73×10^{11}	0.5480	0.0108	0.8843	0.1833
13.33– 16.95	1.74×10^{11}	0.5469	0.0146	0.8845	0.1730
8.33–12.50	1.44×10^{11}	0.5346	0.0106	0.9338	0.1013
8.93–10.10	1.54×10^{11}	0.6500	-0.1420	0.9401	0.1144
7.52–8.33	1.70×10^{11}	0.6000	-0.1781	0.9264	0.1513
6.67–7.52	1.72×10^{11}	0.6000	-0.1781	0.9331	0.1287
3.34–6.67	1.71×10^{11}	0.6009	-0.1304	0.9080	0.1762

4

5

6

1 Table 2. CERES means obtained from Stephens et al. (2012) compared against the
2 MetUM configuration 6.0 means predicted using the B014b parameterization and the
3 temperature-dependent parameterization. All flux units (SW and LW) are in Wm^{-2} .
4 Asterisks denote that the predicted variable is within the current CERES measurement
5 uncertainty.

6

Variable	Observation	B014b	Temperature-dependent
Outgoing SW	100 ± 2	97.58	99.66*
Outgoing LW	239.7 ± 3.3	240.53*	239.52*
Absorbed SW	240.2 ± 2	242.80	240.73*
Albedo TOA	29.41 ± 1	28.67*	29.28*
SW CF	-47.5 ± 3	-42.18	-44.23
LW CF	26.7 ± 4	23.88*	24.74*
Net surf SW	165 ± 6	168.64*	170.92*

7